Supplementary Information

Polyoxometalate-incorporated NiFe-based oxyhydroxides for enhanced oxygen evolution reaction in alkaline media

*Yuyan Qiao[‡ a,b,c], Yanqiu Pan[‡ c], Wenjun Fan[*a], Guifa Long[*d] and Fuxiang Zhang[*a]*

a State Key Laboratory of Catalysis, iChEM, Dalian Institute of Chemical Physics, Chinese Academy of Sciences, Dalian, 116023, China;

Email: wjfan@dicp.ac.cn; fxzhang@dicp.ac.cn

b Jiangxi Province Engineering Research Center of Ecological Chemical Industry, Jiujiang University, Jiujiang, 332005, China

c School of Chemical Engineering, Dalian University of Technology, Dalian, 116024, China;

d Guangxi Key Laboratory of Chemistry and Engineering of Forest Products, School of Chemistry and Chemical Engineering, Guangxi University for Nationalities, Nanning, 530008, China;

Email: gflong@gxmzu.edu.cn

‡ The two authors contributed equally to this work.

Contents

1. Experimental and computational details

1.1. Chemicals and Materials.

All the reagents were analytical grade and used without further purification. Iron nitrate nonahydrate (Fe(NO$_3$)$_3$·9H$_2$O, ≥ 98.5 wt.%), potassium hydroxide (KOH, ≥ 85 wt.%), Ethylene glycol (EG, ≥ 99.5 wt.%), ethanol (EtOH, ≥ 99.7 wt.%), dimethylformamide (DMF, ≥ 99.5 wt.%) and acetone (≥ 99.5 wt.%) were obtained from National Pharmaceutical Industry Corporation Ltd., Shanghai. Nickel nitrate hexahydrate (Ni(NO$_3$)$_2$·6H$_2$O, ≥ 98 wt.%), Phosphomolybdic acid (PMA, AR), and glucose (Glc, AR) were purchased from Sigma-Aldrich Corporation. Carbon fiber paper (CFP, TGP-H-060, Toray) was used as the substrate material of electrodes. Deionized water (DI) water (18.2 MΩ·cm^{-1}) was used for the preparation of all aqueous solution. All the reagents were used directly without further purification.

1.2. Synthesis of catalysts.

In situ **growth of CNTs on CFP.** The preparation is referred to our previous reported work with slight modification using the chemical vapor deposition (CVD) method[1]. Typically, the CFP was ultrasonically treated with ethanol, acetone, and deionized water, followed by oxidation treatment in concentrated HNO$_3$ (65–68%). Afterward, the substrate was impregnated in a mixed solvent of EG and EtOH with trace amount of Ni(NO$_3$)$_2$·6H$_2$O as the catalyst for CNTs generation. Subsequently, this substrate was heated in a furnace tube at 700 °C for 2 h with the 5% H$_2$/Ar gas (100 sccm flow rate) carrying the EtOH vapor at the upstream, which was used as the carbon source for *in situ* generation of CNTs on the CFP electrode. To remove the residue Ni species, the electrode was immersed into HNO$_3$ solution for 3 h. The as-obtained CNTs on CFP were denoted as CNTs/CFP.

Preparation of NiFe-PMA/CNTs on CFP. 0.05 mmol PMA, 1.0 mmol glucose, 0.8 mmol Ni (NO$_3$)$_2$·6H$_2$O and Fe (NO$_3$)$_2$·9H$_2$O were dissolved orderly in 16 mL DMF solution with continuous stirring, and then underwent solvothermal reaction with CNTs/CFP at 140 °C for 12 h. The synthesized electrode was denoted as NiFe-PMA/CNTs. For comparison, NiFe/CNTs, Ni-PMA/CNTs, Fe-PMA/CNTs and PMA/CNTs were synthesized without PMA or Fe(Ni) following the similar process.

Synthesis of IrO$_2$ electrocatalyst. IrO$_2$ powder was prepared by a similar method mentioned in other literatures and used as the benchmark electrocatalyst[2]. The obtained IrO$_2$ micelle was filtered and washed with water, and then dried in a vacuum oven.

1.3. Materials Characterizations.

The phases of the catalysts were examined using on a Rigaku D/Max-2500/PC using Cu-Kα radiation with an operating voltage of 40 kV and current of 200 mA. The morphologies of synthesized samples were assessed by scanning electron microscopy (SEM, Quanta 200 FEG, FEI),

transmission electron microscopy (TEM, Hitachi HT7700) and high-resolution transmission electron microscope (HRTEM, JEOL JEM-F200). The high-resolution aberration-corrected high-angle annular dark-field scanning transmission electron microscopy (AC HAADF-STEM) as well as a energy-dispersive spectroscopy (EDS) detector was acquired on the JEOL JEMARM300F STEM with a energy-dispersive spectroscopy (EDS) detector. Quantitative analysis of elements could be obtained by inductively coupled plasma atomic emission spectrometry (ICP-AES). The constitutions of samples and binding energies were explored by the X-ray photoelectron spectroscopy (XPS, Thermo ESCALAB 250Xi), and the binding energy was referenced to C 1s with at 284.6 eV. The infrared spectroscopy (IR) was measured by HYPERION 3000 spectrometer (Bruker Optics Inc., GER) in the range of 500-4000 cm^{-1}. The X-ray absorption near edge structure (XANES) and extended X-ray absorption fine structure (EXAFS) were collected at 1W1B beamline of Beijing Synchrotron Radiation Facility (BSRF). The data were collected in transmission or fluorescence mode using a Lytle detector. The samples were directly pasted on the special adhesive tape. The EXAFS data were processed according to the standard procedures using the ATHENA module of Demeter software packages. The reference spectra of Fe foil, Fe_2O_3, MoO_2 and MoO_3 were also obtained for comparison.

1.4. Electrochemical Measurements.

The electrochemical tests were performed on a CHI660E electrochemical workstation in O_2-satuated 1.0 M KOH electrolyte in a conventional three-electrode system. The electrochemical impedance spectroscopy (EIS) was performed on a Solartron workstation with the frequency range from 100K Hz to 0.01 Hz. The *in-situ* synthesized electrocatalysts were directly used as working electrodes. For the benchmark IrO_2 catalyst, 5 mg of the prepared IrO_2 was mixed with 450 μL ethanol and 50 μL 5% Nafion solution, and then sonicated for 30 min. Subsequently, 80 μL of the IrO_2 suspension was dropped onto the CNTs/CFP electrode and dried at the infrared light. The loading of IrO_2 was about 0.8 mg cm^{-2}. The Hg/HgO electrode was used as the reference electrode and graphite rod as the counter electrode. The working potentials were calibrated against reversible the hydrogen electrode (RHE), E (V, RHE) = E (Hg/HgO) + 0.098 + 0.059 *pH. And the pH value of aqueous 1M KOH solution is equivalent to 13.6. The polarization curve was carried out at a scan rate of 5 mV·s^{-1} with 90% iR compensation. To evaluate the long-term stability of OER, the chronopotentiometry was tested at 10 mA cm^{-2} in 1.0 M KOH.

The electrochemical active surface area (ECSA) of the electrodes could be determined by dividing the double layer capacitance (C_{dl}) by the specific capacity (C_s)[3]. The C_{dl} was calculated by measuring the capacitive current associated with double-layer charging-discharging from the scan-rate dependence of cyclic voltammetry (CV): $C_{dl} = (j_{anode} - j_{cathode})/2*\nu$, where j_{anode} represents the charging

current, $j_{cathode}$ represents the charging current, and ν is the scan rate. Assuming that all metal atoms were active sites for the samples, the TOF value could be achieved through the equation: TOF = $j*S/4*n*F$, where j represents the current density at a specified potential, S is the surface area of the working electrode, n is the molar number of all metals on this catalyst and F is Faradaic constant (96485 C mol^{-1}). Furthermore, the Faradaic efficiency (FE) could be obtained by the formula: FE=$n*x*F*v/I$, in which n is the electron transfer number, x is the volume fraction of O_2 measured via online gas chromatography based on a calibration curve, F is the Faradaic constant, v is the O_2 gas flow rate, and I is current density during test.

1.5. Computational details

All the density functional theory (DFT) calculations were performed with MedeA VASP using the ab-initio total-energy and molecular dynamics package VASP (Vienna ab-initio simulation package) [4, 5] with electron correction treated within the generalized gradient approximation using the revised Perdew-Burke-Ernzerhof (rPBE) exchange-correlation functional[6, 7]. The projector augmented wave (PAW) method[8] was used to treat the effect of the inner cores on the valence states. In all the calculations, the cutoff energy was set to be 500 eV and Gaussian electron smearing method with σ = 0.05 eV were used. The convergence tolerance for residual force and energy on each atom during structure relaxation was set to 0.05 eV Å^{-1} and 10^{-5} eV, respectively. The Monkhorst-Pack grids[9] were set to be 3 × 3 × 1, 3 × 3 × 1, and 3 × 3 × 1 for computing the structure optimizations of NiFe/CNTs, PMA/CNTs, and NiFe-PMA/CNTs, respectively. A vacuum layer of 20 Å along the z direction was introduced to eliminate the spurious interactions between adjacent sheets. The DFT-D3 method[10] was adopted to consider van der Waals correction.
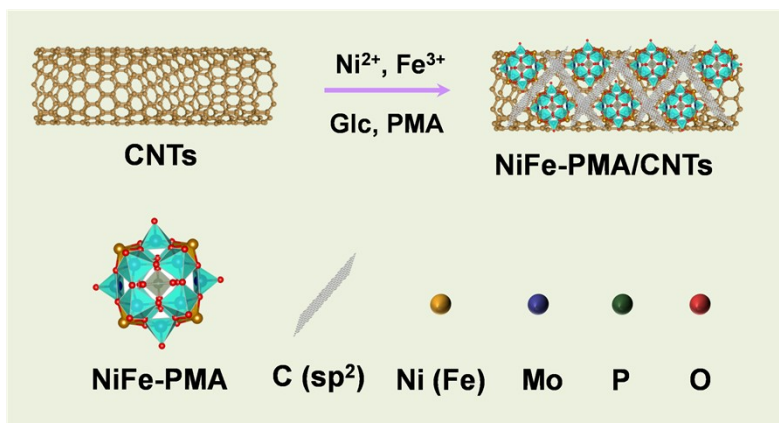
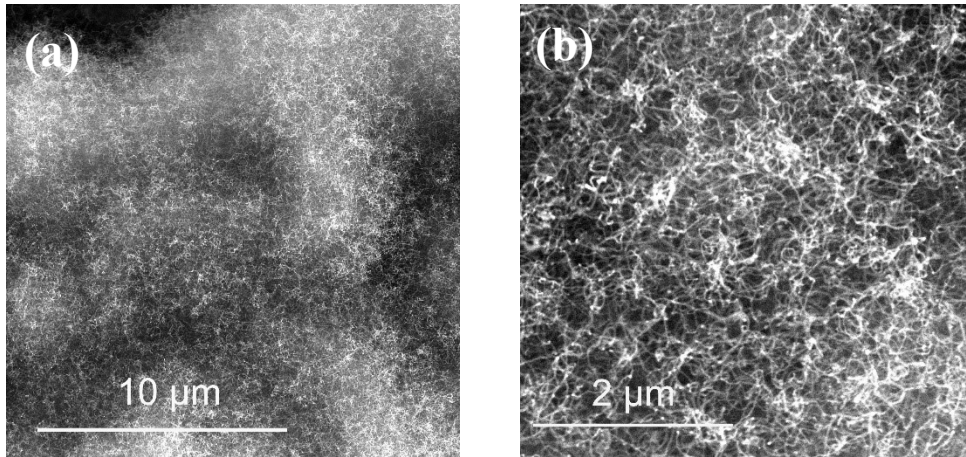**Figure S1**. Schematic process of synthesizing NiFe-PMA/CNTs electrocatalyst.

Figuer S2. (a) SEM and (b) Enlarged SEM images of CNTs/CFP.
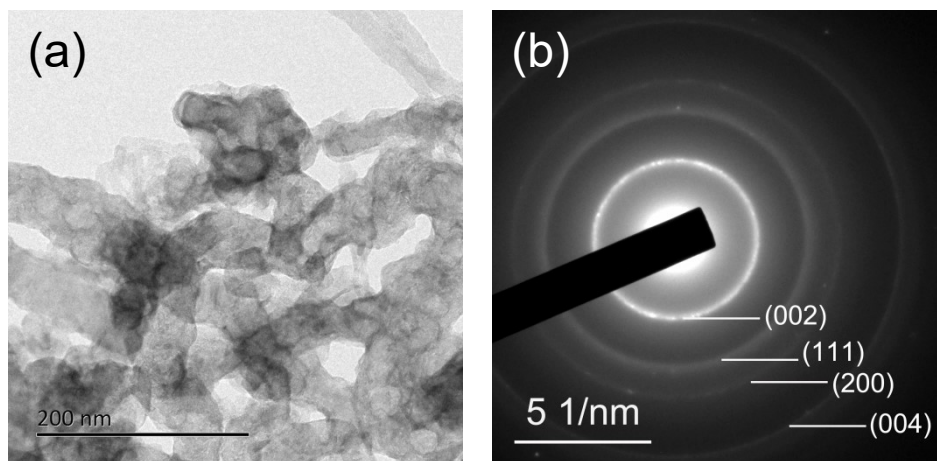
Figure S3. (a) HRTEM images of NiFe-PMA/CNTs. (b) The Selected area electron diffraction (SAED) images of NiFe-PMA/CNTs. The diffraction rings matched with the (002), (004) plane of graphite-2H (PDF#: 41-1487) and the (111), (200) plane of metallic Ni (PDF: 04-0850).
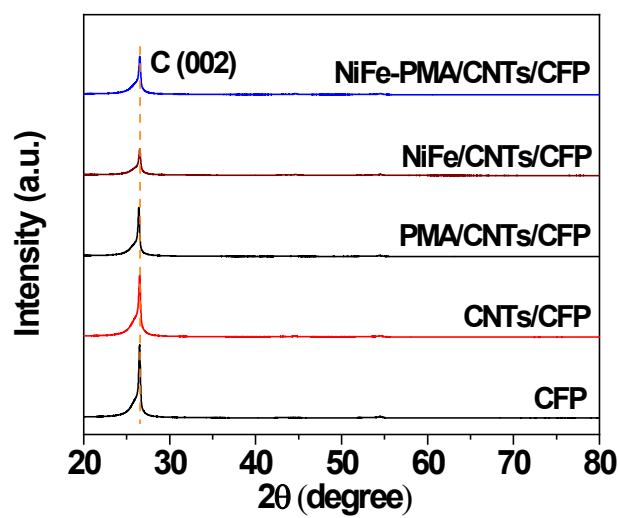
Figure S4. XRD patterns of CFP, CNTs/CFP, PMA/CNTs/CFP, NiFe/CNTs/CFP, and NiFe-PMA/CNTs/CFP.
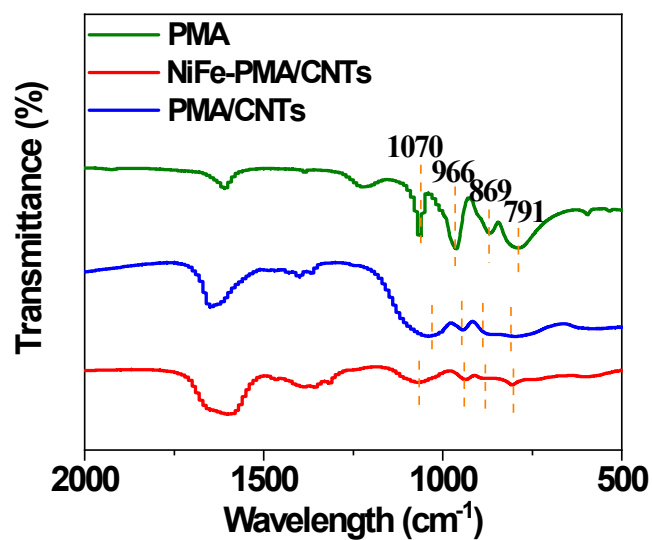
Figure S5. FTIR spectra of PMA, PMA/CNTs, and NiFe-PMA/CNTs. The characteristic peaks at 1070, 966, 869, 791 cm^{-1} can be ascribed to P−O, Mo=O, Mo−O$_c$−Mo (corner-sharing oxygen) and Mo−O$_e$−Mo (edge-sharing oxygen), respectively.
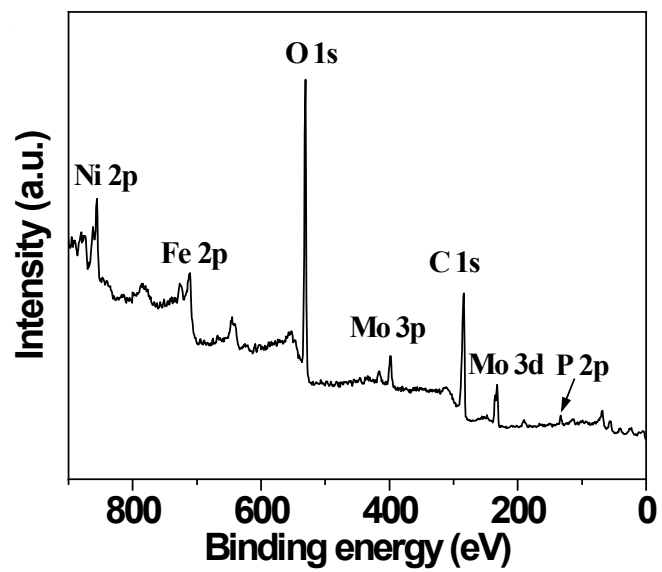
Figure S6. The XPS survey spectra of NiFe-PMA/CNTs.
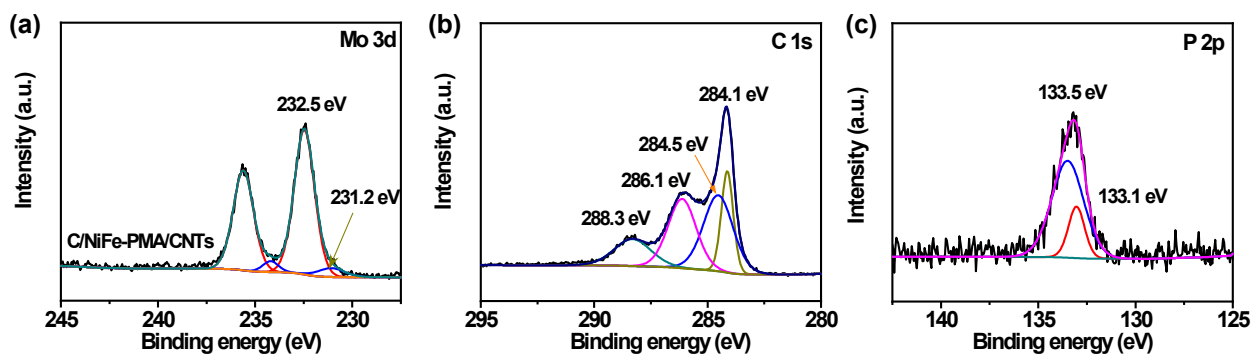
Figure S7. (a) Mo 3d, (b) C 1s, (c) P 2p XPS spectra for NiFe-PMA/CNTs.

Note: In addition, the deconvolution of Mo 3d spectrum for NiFe-PMA/CNTs in Figure 2c yields two components, the one with the main peak of $3d_{3/2}$ at 231.2 eV for Mo^{4+} and the other at 232.5 eV for Mo^{6+}, respectively. Correspondingly, the O 1s spectrum consisted of two main peaks at 531.3 eV for oxygen species in M−OH (M = Ni, Fe) and 533.1 eV for Mo-O in PMA, respectively (Figure S7a). Four peaks in Figure 2e could be distinguished from the C 1s spectrum in Figure S7b, including C (sp^2) (284.1 eV), C-C (284.5 eV), C-OH (286.1 eV) and O-C=O (288.3 eV), respectively. The two peaks of the P 2p spectrum in Figure S7c were attributed to P-C (133.1 eV) and P-O (133.5 eV) species, demonstrating the interface interaction between carbon materials and PMA.
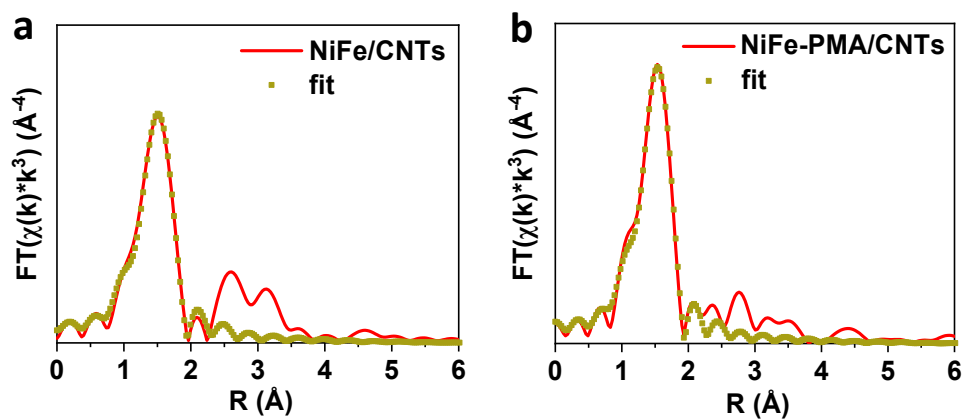
Figure S8. Comparisons of Fourier transform spectra and the fitting curves. (a) NiFe/CNTs, and (b) NiFe-PMA/CNTs.
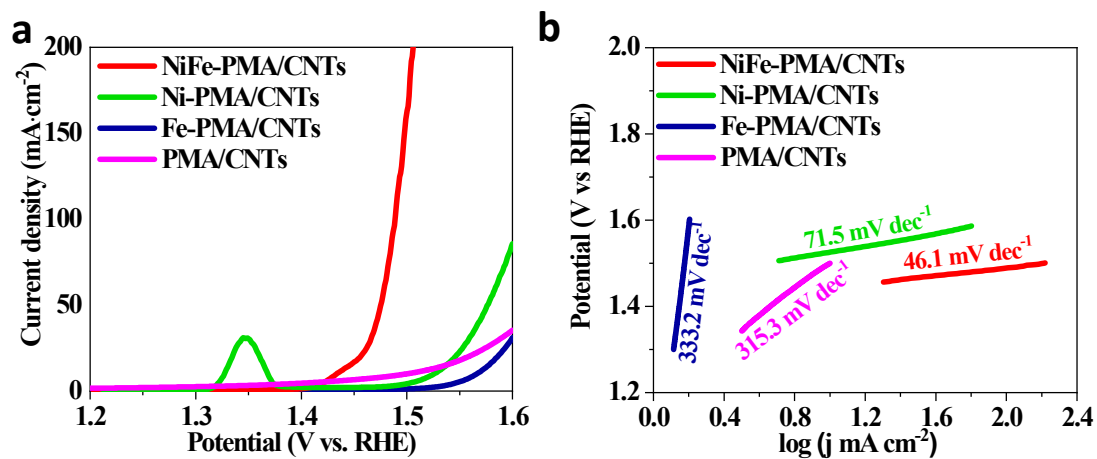
Figure S9. (a) LSV curves, and (b) Tafel plots of PMA/CNTs, Fe-PMA/CNTs, Ni-PMA/CNTs, and NiFe-PMA/CNTs in 1 M KOH, respectively.
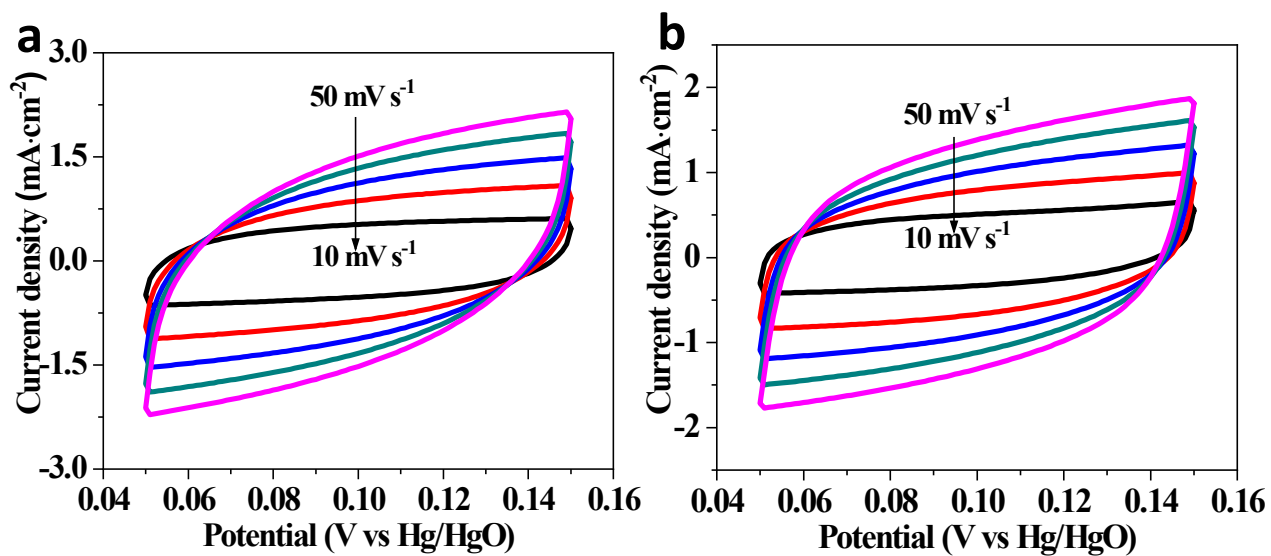
Figure S10. CV curves for different electrocatalysts in 1 M KOH electrolyte with the range from 0.05 to 0.15 V (vs Hg/HgO). (a) NiFe/CNTs, and (b) NiFe-PMA/CNTs.
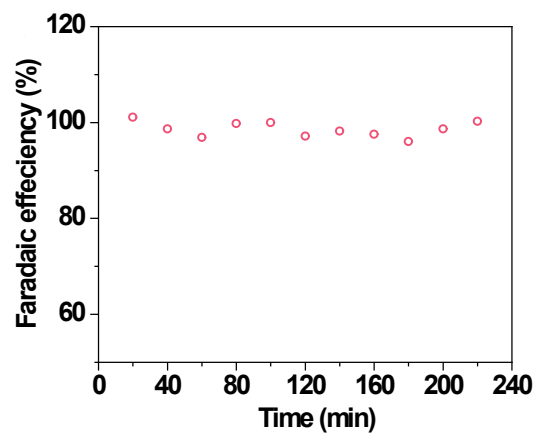
Figure S11. The Faradaic Efficiency of NiFe-PMA/CNTs/CFP in 1M KOH at 10 mA cm^{-2}.
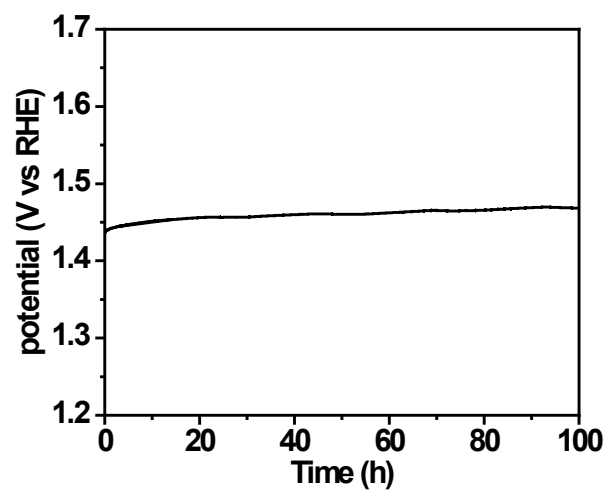
Figure S12. Chronopotentiometry curve of NiFe /CNTs at 10 mA cm^{-2} in 1 M KOH.
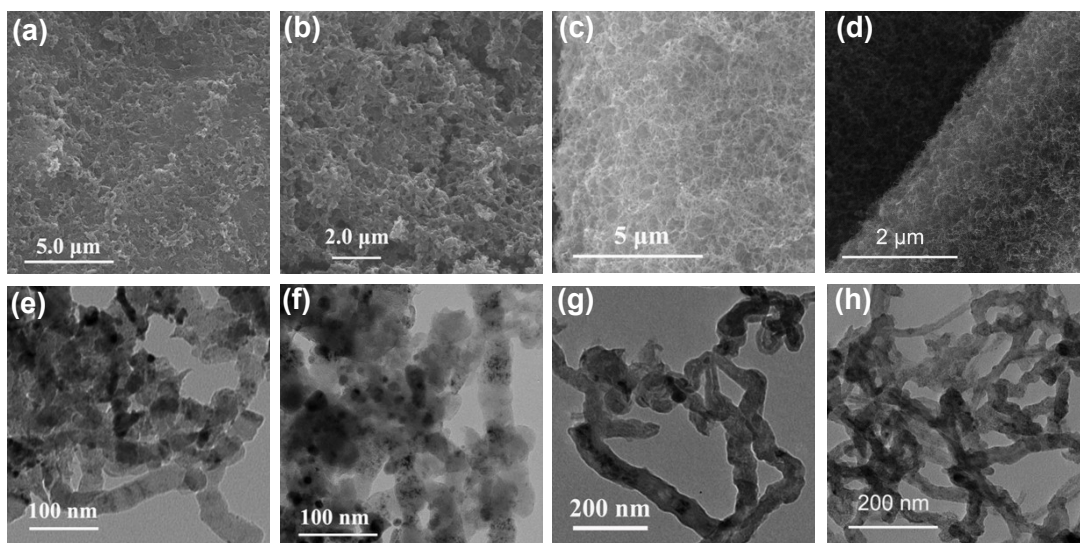
Figure S13. SEM images before and after stability for: (a, b) NiFe/CNTs, and (c, d) NiFe-PMA/CNTs. TEM images before and after stability for: (e, f) NiFe/CNTs, and (g, h) NiFe-PMA/CNTs.
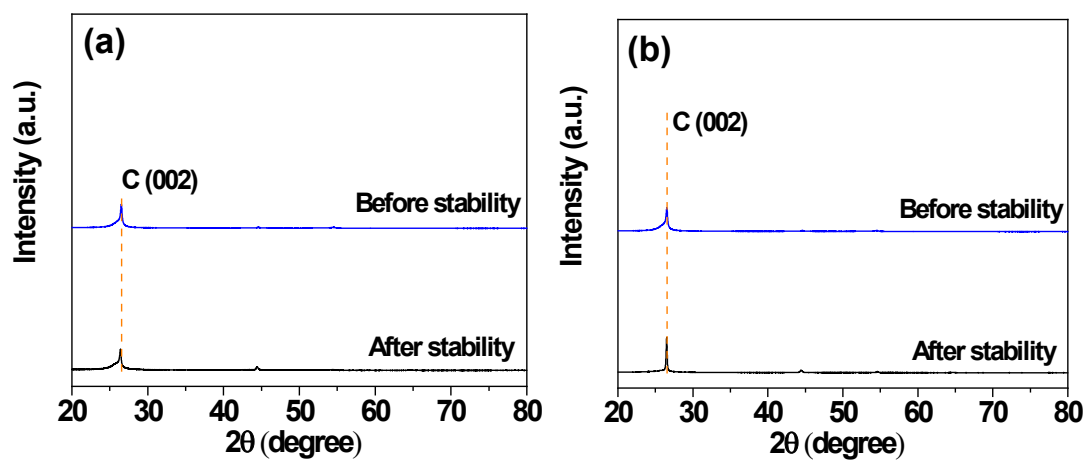
Figure S14. XRD patterns. (a) NiFe/CNTs, and (b) NiFe-PMA/CNTs before and after stability.
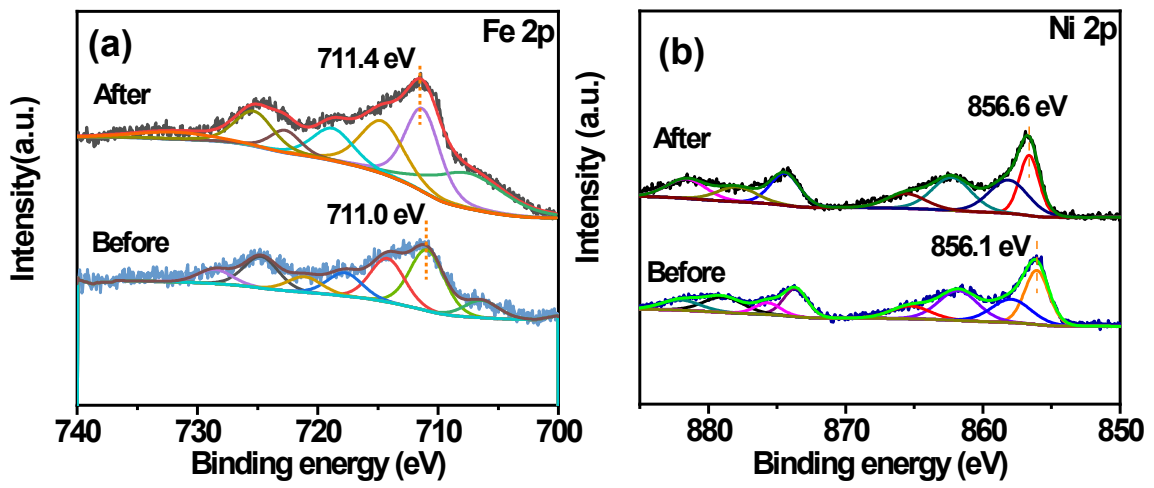
Figure S15. XPS spectra for NiFe/CNTs. (a) Fe 2p, and (b) Ni 2p before and after stability.
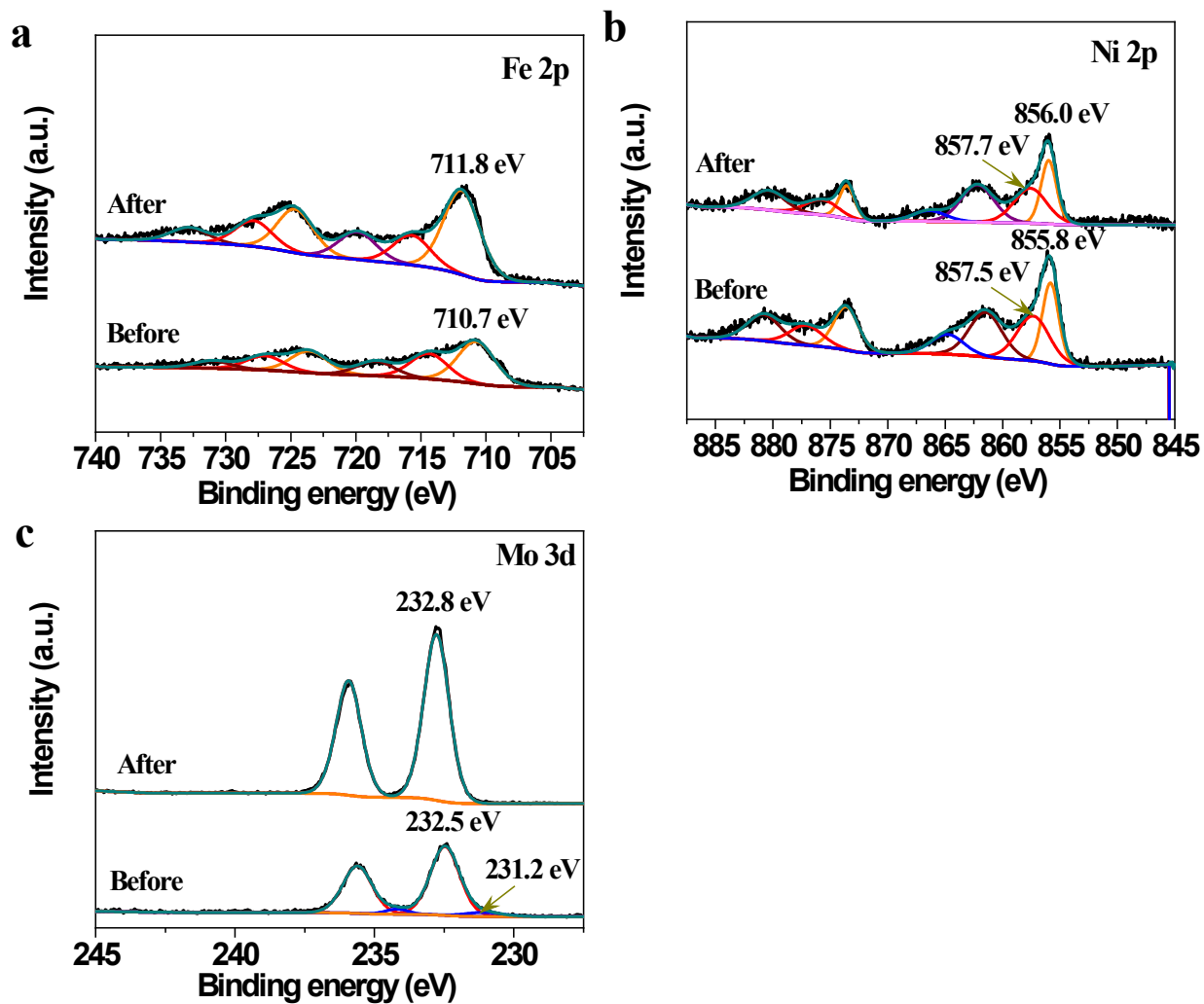
Figure S16. XPS spectra for NiFe-PMA/CNTs. (a) Fe 2p, (b) Ni 2p, and (c) Mo 3d before and after stability.

a PMA/CNTs

b NiFe/CNTs
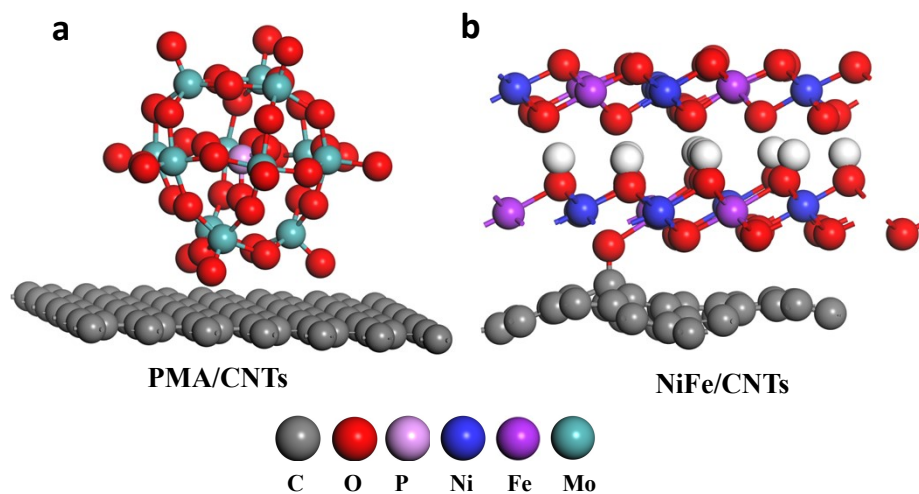
C   O   P   Ni   Fe   Mo

Figure S17. Optimized structures of PMA/CNTs and NiFe/CNTs. The balls in grey, red, pink, blue, violet and cyan represent C, O, P, Ni, Fe and Mo atoms, respectively.

Table S1. The composition of NiFe-PMA/CNTs detected by ICP-OES. M represents the weight of catalyst supported onto the substrates for samples, mg cm^{-2}.

Sample	Ni (mmol·cm^{-2})	Fe (mmol·cm^{-2})	Mo (mmol·cm^{-2})	M (mg·cm^{-2})
NiFe-PMA/CNTs	6.4×10^{-4}	6.7×10^{-4}	3.8×10^{-4}	0.80
NiFe/CNTs	7.1×10^{-4}	1.2×10^{-3}	-	1.50
PMA/CNTs	-	-	1.3×10^{-3}	0.40

Table S2. Corresponding fitting results of the first coordinate shell about Fe K-edge XANES spectra

Sample	Shell	N	R (Å)	σ^2 (10^{-3} Å^2)	ΔE_0 (eV)	R factor (%)
Fe foil	Fe-Fe	8	2.46 ± 0.02	4.6 ± 1.9	4.66 ± 2.39	0.6
Fe$_2$O$_3$	Fe-O$_1$	3	1.93 ± 0.04	3.2 ± 0.8	-1.55 ± 4.17	1.1
	Fe-O$_2$	3	2.10 ± 0.05	5.9 ± 0.9		
NiFe/CNTs	Fe-O	6.0 ± 0.3	2.0 ± 0.01	6.2 ± 0.8	-0.08 ± 0.52	0.1
NiFe-PMA/CNTs	Fe-O	5.9 ± 0.4	2.0 ± 0.01	6.5 ± 0.1	-2.01 ± 0.97	0.2

for NiFe/CNTs and NiFe-PMA/CNTs, respectively.

Table S3. Fitting results of the first coordinate shell of Mo K-edge XANES spectra for NiFe/PMA/CNT and reference samples, respectively.

Sample	Shell	N	R (Å)	$\sigma^2 (10^{-3} Å^2)$	ΔE_0 (eV)	R factor(%)
Mo foil	Mo-Mo$_1$	8	2.71 ± 0.01	3.3±1.5	2.98 ± 1.49	1.0
	Mo-Mo$_2$	6	3.12 ± 0.01	2.9±0.1		
MoO$_2$	Mo-O$_1$	2	1.90 ± 0.03	3.0±0.2	-1.65 ± 2.70	1.1
	Mo-O$_2$	4	2.2 ± 0.01	3.0±0.2		
MoO$_3$	Mo-O$_1$	1	1.68 ± 0.01	4.5	-7.02 ± 7.01	1.6
	Mo-O$_2$	1	1.82 ± 0.02	4.5		
	Mo-O$_3$	2	1.96 ± 0.01	4.5		
	Mo-O$_4$	1	2.14 ± 0.02	4.5	-1.55 ± 4.17	1.1
NiFe-PMA/CNTs	Mo-O$_1$	0.9 ± 1.1	1.70 ± 0.01	6.0 ± 0.1	-2.93 ± 1.50	3.0
	Mo-O$_2$	0.7 ± 0.4	1.84 ± 0.02	6.0 ± 0.1		

Table S4. Comparison of OER activities for NiFe/PMA and other non-noble metal electrocatalysts in alkaline electrolyte.

Material	Overpotential at 10 mA cm^{-2} (mV)	TOF (s^{-1})	Electrolyte	Reference
NiFe-PMA/CNT	~203	2.34	1 M KOH	This work
NiFe-LDH/CNT	~230	0.56	1 M KOH	[11]
TANF	280	1.36	1 M KOH	[12]
G-FeCoW	223	0.46	1 M KOH	[13]
FeNi(MoO$_4$)$_x$@NF	227	0.51	1 M KOH	[14]
FeCoNiP	200	0.47	1M KOH	[15]
Cr^{6+}@G	197	0.92	1 M KOH	[16]
a/c-NiFe-G	217	0.87	1 M KOH	[17]
Fe-Co$_3$O$_4$	262	0.0169	1 M KOH	[18]
F-NiFe-A	218	~0.25	1 M KOH	[19]
Fe(PO$_3$)$_2$/Ni$_2$P	177	0.12	1 M KOH	[20]

Note: The overpotentials in Column II was measured at 10 mA cm^{-2} and the TOF values in Column III was calculated at 1.53 (V vs. RHE).

Table S5. The fitting results of EIS data at 1.58 (V vs RHE) for C/NiFe/CNTs, and NiFe-PMA/CNTs.

sample	R_1 (Ω)	R_2 (Ω)	CPE-T	CPE-P
C/NiFe /CNTs	1.7	2.2	0.0446	0.836
NiFe-PMA/CNTs	1.8	1.0	0.109	0.883

Table S6. ICP-OES results for KOH electrolyte before and after 100 h stability test.

Conditions	Ni (µg/L)	Fe (µg/L)	Mo (µg/L)
Before stability	0	0.0385	0.0004
After stability	0	0.0556	0.00217

References

1. Y. Qiao, Y. Pan, S. Du, T. Wu, Y. Cao, G. Long, W. Fan and F. Zhang, *J. Phys. Chem. C*, 2021, **125**, 26003-26012.
2. F. Zhang, K. Maeda, T. Takata, T. Hisatomi and K. Domen, *Catal. Today*, 2012, **185**, 253-258.
3. C. C. L. McCrory, S. Jung, J. C. Peters and T. F. Jaramillo, *J. Am. Chem. Soc.*, 2013, **135**, 16977-16987.
4. Kresse and Hafner, *Phys. Rev. B Condens. Matter*, 1993, **47**, 558-561.
5. Kresse and Furthmuller, *Phys. Rev., B Condens. Matter*, 1996, **54**, 11169-11186.
6. Perdew and Wang, *Phys. Rev., B Condens. Matter*, 1992, **45**, 13244-13249.
7. L. B. H. B. Hammer, J. K. No"rskov, *Phys. Rev. B*, 1999, **59**.
8. Blochl, *Phys. Rev., B Condens. Matter*, 1994, **50**, 17953-17979.
9. H. J. Monkhorst and J. D. Pack, *Phys. Rev. B*, 1976, **13**, 5188-5192.
10. P. W. Menezes, A. Indra, I. Zaharieva, C. Walter, S. Loos, S. Hoffmann, R. Schloegl, H. Dau and M. Driess, *Energy & Environ. Sci.*, 2019, **12**, 988-999.
11. M. Gong, Y. Li, H. Wang, Y. Liang, J. Z. Wu, J. Zhou, J. Wang, T. Regier, F. Wei and H. Dai, *J. Am. Chem. Soc.*, 2013, **135**, 8452-8455.
12. Y. Shi, Y. Yu, Y. Liang, Y. Du and B. Zhang, *Angew. Chem.Int. Edit.*, 2019, **58**, 3769-3773.
13. B. Zhang, X. Zheng, O. Voznyy, R. Comin, M. Bajdich, M. Garcia-Melchor, L. Han, J. Xu, M. Liu, L. Zheng, F. P. G. de Arquer, C. T. Dinh, F. Fan, M. Yuan, E. Yassitepe, N. Chen, T. Regier, P. Liu, Y. Li, P. De Luna, A. Janmohamed, H. L. Xin, H. Yang, A. Vojvodic and E. H. Sargent, *Science*, 2016, **352**, 333-337.
14. K. Dastafkan, S. Wang, C. Rong, Q. Meyer, Y. Li, Q. Zhang and C. Zhao, *Adv. Funct. Mater.*, 2021, **32**, 202107342.
15. J. Xu, J. Li, D. Xiong, B. Zhang, Y. Liu, K.-H. Wu, I. Amorim, W. Li and L. Liu, *Chem. Sci.*, 2018, **9**, 3470-3476.
16. Y. Yao, Z. Xu, F. Cheng, W. Li, P. Cui, G. Xu, S. Xu, P. Wang, G. Sheng, Y. Yan, Z. Yu, S. Yan, Z. Chen and Z. Zou, *Energy & Environ. Sci.*, 2018, **11**, 407-416.
17. Z. Gong, R. Liu, H. Gong, G. Ye, J. Liu, J. Dong, J. Liao, M. Yan, J. Liu, K. Huang, L. Xing, J. Liang, Y. He and H. Fei, *ACS Catal.*, 2021, **11**, 12284-12292.
18. S. L. Zhang, B. Y. Guan, X. F. Lu, S. Xi, Y. Du and X. W. Lou, *Adv. Mater.*, 2020, **32**, e2002235.
19. Q. Xu, H. Jiang, X. Duan, Z. Jiang, Y. Hu, S. W. Boettcher, W. Zhang, S. Guo and C. Li, *Nano Lett.*, 2021, **21**, 492-499.
20. H. Zhou, F. Yu, J. Sun, R. He, S. Chen, C.-W. Chu and Z. Ren, *Proc. Nat. Aca. Sci. Unit. Stat. Am.*, 2017, **114**, 5607-5611.